HHS Public Access

Author manuscript

J Am Soc Echocardiogr. Author manuscript; available in PMC 2023 September 01.

Published in final edited form as:

J Am Soc Echocardiogr. 2022 September ; 35(9): 985–996.e11. doi:10.1016/j.echo.2022.04.015.

Visualization and Quantification of the Unrepaired Complete Atrioventricular Canal Valve using Open-Source Software

Hannah H. Nam, BA[1], **Christian Herz, MS**[1], **Andras Lasso, PhD**[2], **Alana Cianciulli, BS**[1], **Maura Flynn, BS**[1], **Jing Huang, PhD**[3], **Zi Wang, MS**[3], **Beatriz Paniagua, PhD**[4], **Jared Vicory, PhD**[4], **Saleha Kabir, MD**[5], **John Simpson, MD**[5], **David Harrild, MD, PhD**[6], **Gerald Marx, MD**[6], **Meryl S. Cohen, MD**[7], **Andrew C. Glatz, MD MSCE**[7,8], **Matthew A. Jolley, MD**[1,7]

[1]Department of Anesthesiology and Critical Care Medicine, Children's Hospital of Philadelphia, Philadelphia, PA

[2]Laboratory for Percutaneous Surgery, Queen's University, Kingston, ON

[3]Department of Biostatistics, Epidemiology, and Informatics, University of Pennsylvania, Philadelphia, PA

[4]Kitware, Inc, Clifton Park, NY.

[5]Department of Congenital Heart Disease, Evelina London Children's, Hospital, UK

[6]Department of Cardiology, Boston Children's Hospital, Boston, MA.

[7]Division of Pediatric Cardiology, Children's Hospital of Philadelphia, Philadelphia, PA

[8]Center for Pediatric Clinical Effectiveness, Children's Hospital of Philadelphia, Philadelphia, PA

Abstract

Background-—Repair of complete atrioventricular canal (CAVC) is often complicated by residual left atrioventricular valve regurgitation (AVVR). The structure of the mitral and tricuspid valves in biventricular hearts has previously been shown to be associated with valve dysfunction. However, the three-dimensional (3D) structure of the entire unrepaired CAVC valve has not been quantified. Understanding the 3D structure of the CAVC may inform optimized repair.

Methods-—We created novel open-source workflows in SlicerHeart for the modeling and quantification of CAVC valves based upon 3D echocardiogram (3DE) images. We applied these methods to model the annulus, leaflets, and papillary muscle structure of 35 patients (29 with Trisomy 21) with CAVC using transthoracic 3D echocardiograms. The mean leaflet and annular shapes were calculated and visualized using shape analysis. Metrics of the complete native CAVC valve structure were compared to normal mitral valves, using the Mann-Whitney U test. Associations between CAVC structure and AVVR were analyzed.

Results-—CAVC leaflet metrics vary throughout systole. Compared to normal mitral valves, the left CAVC PMs are more acutely angled in relation to the annular plane ($p<0.001$). In addition,

Corresponding Author: Matthew Jolley, Children's Hospital of Philadelphia, 3401 Civic Center Blvd, Philadelphia, PA 19104, Phone 267-426-8794, JOLLEYM@email.chop.edu.

Disclosures: Beatriz Paniagua and Jared Vicory are employees of Kitware Inc.

the antero-lateral PM is laterally and inferiorly rotated in CAVC, while the postero-medial PM is more superiorly and laterally rotated, relative to normal mitral valves($p<0.001$). Lower native CAVC atrioventricular valve annular height and annular height-to-width ratio (AHWR) prior to repair are both associated with moderate or greater left atrioventricular valve (LAVV) regurgitation after repair ($p<0.01$).

Conclusions-—It is feasible to model and quantify 3D CAVC structure using 3DE images. We demonstrate significant variation in CAVC structure across the cohort and differences in annular, leaflet and PM structure compared to the mitral valve. These tools may be used in future studies to catalyze future research intended to identify structural associations of valve dysfunction and to optimize repair in this vulnerable and complex population.

Subject Terms:

Congenital Heart Disease; Echocardiography; Valvular Heart Disease

INTRODUCTION

In the current era, complete atrioventricular canal(CAVC) repair is typically performed in early childhood. Despite low operative mortality, hemodynamically significant atrioventricular valve regurgitation (AVVR) occurs in up to 40% of patients, with suboptimal results after surgical reintervention.[1–4]

In adults, the understanding of the dynamic three-dimensional (3D) structure of the mitral and tricuspid valve has been significantly informed by 3D echocardiography (3DE) and 3DE-based modeling.[5–7] Numerous studies have demonstrated that the architecture of the mitral valve leaflets, annulus, and papillary muscles (PM) are all associated with regurgitation in both children and adults, and that the assessment of preoperative leaflet structure can predict durability of repair.[8–10]

Left atrioventricular valve structure after CAVC repair is a product of both the native unrepaired CAVC valve structure, and the surgical repair technique. As such, a detailed understanding of the native CAVC valve structure may inform design and method of surgical repair, which in turn may lead to improved outcomes.[11–13] However, to date there has not been an accessible tool for quantitative 3D modeling of the native, unrepaired CAVC valve before repair. We have previously performed an analysis of the native CAVC annulus but at the time were unable to analyze the individual leaflets and subvalvular structure.[14] This deficit prevented a quantitative, 3D image-derived exploration of the structure of the complete native CAVC valve. In this study, our primary goal was to develop the capability to model, visualize, and quantify the CAVC valve leaflets and papillary muscles, and apply the tools to characterize the native CAVC valve structure using 3DE. We hypothesized that CAVC leaflet, and PM structure differ from normal mitral valves, and that these tools could be used to identify relationships of CAVC structure to LAVV regurgitation after repair.

MATERIAL AND METHODS

Subjects

Institutional databases at the Children's Hospital of Philadelphia (CHOP), Boston Children's Hospital, and Evelina London were used to identify patients with CAVC in whom transthoracic apical 4 chamber 3DE had been collected for clinical studies. To augment these studies, dedicated acquisitions in the operating room prior to repair were obtained at CHOP. These studies were obtained with parental consent per an institutional review board (IRB) approved protocol. For a control group, 3DE of the mitral valves of young children without known pathology and otherwise normal echocardiograms (echo) were identified as prior.[15] Schematic comparisons between normal heart anatomy and CAVC anatomy are depicted in Fig 1. Exclusion criteria for all studies included presence of significant stitch artifact, lack of inclusion of the entire CAVC valve in the acquisition or inability to delineate the individual valve leaflets clearly. This study was performed according to a protocol approved by the IRB at the Children's Hospital of Philadelphia.

Transthoracic Image Acquisition

3DE images were acquired using Full Volume gated acquisitions. Transthoracic X7 or X5 probes were used with the Philips IE33 and EPIQ 7 ultrasound systems (Philips Medical, Amsterdam, Netherlands). The frame rate of the acquisitions ranged from 25 – 43 Hz. Qualitative assessment of ventricular function and degree of AVVR were drawn from clinical interpretations by attending physicians at the time the study was acquired. Post -repair studies were performed prior to discharge from the hospital. Grading of AVVR before and after repair was performed by a single observer. Identification of Rastelli type was drawn from clinical reports and confirmed by visual inspection of the 2D and 3D echo images.

Annular Curve Modeling and Quantification

Annular modeling was performed analogously to our previous descriptions, but was performed using the new CAVC, mitral, and tricuspid presets in the *Valve Annulus Analysis* module in SlicerHeart(Video 1, Figure 2B and 2C).[14, 16] In total, 4 equally spaced cardiac phases were modeled for CAVC, mitral, and aortic valves (End-diastole[ED], Mid-Systole[MS], End-Systole (ES), and Mid-Diastole[MD]). Annular metrics, annular height to valve width ratio (AHWR), and Procrustes analyses were calculated as previously described (Supplemental Figures S1, S2, S3, S4).[14, 16]

Leaflet Modeling

After defining the annular curve, the superior bridging leaflet, inferior bridging leaflet, right mural leaflet, and left mural leaflet were individually segmented in ED, MS, and ES by creating a CAVC modeling framework in the *Valve Segmentation* module in SlicerHeart (Fig 2D, 2E, and 2F, Video 1). Leaflet segmentation took 1–3 hours for an experienced research assistant. All metrics were calculated using this new functionality in the *Valve Quantification* module in SlicerHeart (Video 2). Individual leaflet areas were calculated by semi-automatically extracting the surface of the leaflets. The total leaflet area was

calculated two ways: by summing the areas of the individual leaflets (including coaptation surfaces), and by extracting the “atrial” surface of the valve (excluding coaptation surfaces). Coaptation surface area was defined as the area of coaptation between two adjacent leaflets (Fig 3B, Video 2). Mean coaptation height was defined as the average height of coaptation (Fig 3B). The “soap bubble” annular surface was used to define the boundary between tenting volume and billow volume(Fig 3C), as previously described.[6, 9]

Papillary Muscle Modeling

The PM base point, tip point, and chordal insertion points were placed for the normal mitral and left side of the CAVC in MS using the new *Valve Papillary Analysis* tool in SlicerHeart(Video 2). The PM angle was then characterized using two classes of metrics: 1) the PM angle relative to the annular plane, and 2) the rotational angle of the PM within the left ventricle. Different nomenclature has been used to describe the left side papillary muscles in CAVC. For the purposes of consistency in our comparison to the normal mitral PM, we refer to the supero-lateral and infero-medial PM of the CAVC as antero-lateral and postero-medial, respectively.

The PM base to annulus plane angle was defined as the angle between the annular plane and the line connecting the base of the PM to the chordal insertion point on the coaptation of the leaflets(Fig 4A).

Two separate PM rotational angles were computed which were designed to mimic previous explorations using 2D metrics[17, 18]. Both methods used a reference frame created by a line between the center point of the right side and the center point of the left side of the CAVC annulus (for CAVC) or the center points of the mitral and tricuspid valves (for normal controls). The septal point-based PM rotational angle was calculated as shown in Figure 4B. For the center point-based PM rotation angle was calculated as shown in Figure 4C. The antero-lateral and postero-medial PM were modeled for the normal mitral and left side of the CAVC in MS using all three methods.

Shape Analysis—We utilized Spherical Harmonic (SPHARM) Point Distribution Models (PDM) shape parameterization tools in SlicerSALT to calculate the mean leaflet shape of the CAVC leaflet model population (Video 3).[19, 20] We also applied principal component analysis to identify the major modes of variation in the CAVC valves and highlight variation in shape across the population(Video 3).[19, 21]

Statistics

Annular area measures were normalized to body surface area (BSA), and linear measures (e.g. annular diameter) were normalized to $BSA^{0.5}$.[16, 22] Leaflet area and volume measures were normalized to BSA. Continuous variables are presented as median [IQR]. Friedman’s Test was utilized to compare leaflet metrics throughout the cardiac cycle. Comparisons of continuous variables between categorical variables were made using Mann-Whitney U-test. Intra-observer and inter-observer agreement for 17 annular measurements has been previously described. Similarly intra-observer and inter-observer agreement for 15 leaflet measurements were taken on 8 different 3DE datasets modeling in MS. The results

were analyzed using intraclass correlation coefficients (ICC). All analysis was performed using RStudio version 1.1.456 (R Studio, Inc., Boston, MA).

RESULTS

The CAVC leaflets were modeled in ED, MS, and ES in all 35 patients. PM analysis was performed in 34 of the 35 CAVC patients in MS. The median age of the CAVC patients at echo was 0.3 years [IQR 0.2–0.3 years]. Twenty patients had Rastelli type A, and 15 patients had Rastelli type C anatomy. Twenty-nine of the 35 patients had Trisomy 21. Thirty-two patients had qualitatively normal left ventricular systolic function, 2 had mildly diminished left ventricular systolic function, and 1 had moderately diminished left ventricular function prior to repair. Twenty-five patients had trivial/mild and 10 patients had moderate/severe AVVR prior to repair. Thirty-four of the 35 patients underwent CAVC repair. Twenty-one patients had trivial/mild and 13 patients had moderate/severe left sided AVVR after repair (Table 1). Five out of the 13 patients with post-op moderate or worse left AVVR had pre-existing pre-op moderate or worse AVVR. Two out of 6 patients with post-op moderate or worse right AVVR had pre-existing pre-op moderate or worse AVVR.

Characterization of CAVC Native Structure and Comparison to Normal Mitral Valves

Leaflet Analysis—An example of a segmented model of the individual CAVC valve leaflets is shown in Fig 3A. The CAVC total and individual atrial leaflet areas, billow volume, billow height, tenting volume, and tenting height all varied significantly throughout the cardiac cycle (Table 2). The average individual leaflet areas relative to the total valve area were: superior bridging leaflet -- 41%, the inferior bridging leaflet -- 28%, the right mural leaflet -- 17%, and the left mural leaflet -- 14%. Reproducibility of leaflet modeling was excellent (Table S1).

The mean leaflet shapes and principal components of variation in each phase are shown in Video 3. Individual leaflet models are then shown projected across the first two principal components to demonstrate variability in shape across the population.

Papillary Muscle Analysis—The CAVC antero-lateral and postero-medial PM had smaller angles relative to the annular plane (more laterally directed) compared to the normal mitral valve ($p<0.001$). Both metrics of PM rotational position demonstrated differences in CAVC compared to the normal mitral valve (Table 3). As viewed from the ventricle both the antero-lateral and postero-medial CAVC PM were more laterally located and closely spaced ($p <0.001$). All results are shown in Table 3.

Annulus Analysis—The median[IQR] of the total normalized annular area of the normal mitral and normal tricuspid valve complex (11.9 cm^2/m^2 [10.8–13.4]) was significantly smaller than the median[IQR] of the total annular area for the CAVC (19.6 cm^2/m^2 [18.0–23.7]) in MS ($p<0.001$). Compared to the normal mitral valve, the CAVC annulus height was significantly smaller and annular width was significantly larger, resulting in a smaller AHWR (more planar shape) in all phases (Table S2). The mean annular shapes and principal components of variation in each phase for this cohort are shown in Supplemental Figures

S2–S4. Annular metrics analogous to our previous annular analysis are further summarized in Table S2 and S3 to provide a complete assessment of the CAVC.

Association of Pre-Repair CAVC Structure to Pre-Repair and Post Repair AVVR

We preliminarily investigated associations of CAVC 3D structure to AVVR. There were no significant differences in global or individual leaflet area, billow volume, billow height, tenting volume, or tenting height between native CAVC valves with mild or less AVVR and moderate or greater AVVR (Table S4, S5, S6). Similarly, we demonstrated no significant association of PM angle relative to the annulus, or rotational position to pre- or postoperative AVVR (Table 4).

However, the total pre-repair annular height and AHWR in MS was less in patients with moderate/severe post-repair AVVR compared to patients with trivial/mild post-repair left AVVR ($p=0.01$, Table 5, Table S3). In addition, the minimum left-sided coaptation height in MS prior to repair was greater in patients with mild or less left AVVR compared to patients with moderate or greater left AVVR ($p = 0.04$), and the mean LAVV coaptation height trended similarly($p<0.1$) (Table 5, Table S7).

DISCUSSION

We present a novel 3DE-based modeling workflow which we have used to visualize and quantify the native CAVC valve prior to repair. Our major findings are that: 1) modeling of the native CAVC valve annulus, leaflets, and PM from 3DE is feasible using our newly released open-source framework; 2) both the PM angle relative to the annulus and the papillary rotational positions in CAVC differ from normal mitral valves and; 3) the CAVC annulus is flatter than a normal mitral valve; 4) a more planar native CAVC annulus in mid-systole prior to repair may be associated with the presence of moderate or greater LAVV regurgitation after repair.

Structure of CAVC Atrioventricular Valve in Comparison to Normal Mitral Valve

Leaflet Anatomy—To our knowledge this is the first 3D imaging-derived characterization of the leaflets in the native CAVC valve *before* repair and the first to quantify 3D CAVC leaflet metrics in this unique population. We found that on average the superior bridging leaflet is largest, followed by inferior bridging, right mural, and left mural leaflet. However, there is significant variation in the structure of the CAVC leaflets as demonstrated with shape analysis.

The CAVC LAVV after repair is the product of both the native valve anatomy and the surgical modification of the native anatomy to create two valves from one. We modeled the native CAVC valve *before* repair. Notably, Takahashi et al. previously examined the 3D structure of the CAVC LAVV *after* repair.[23] The analyses allow comparison, but did differ in additional ways. While our study focused only on CAVC, Takahashi et al. was comprised of 30 patients with partial atrioventricular canal(AVC)(e.g. primum atrial septal defect and cleft mitral valve), and 23 patients with CAVC.[23] While we normalized our metrics to appropriate indices of BSA, they normalized their linear values to ventricular length. In addition, their methods were comprised of a mixture of a commercial modeling program

intended for the mitral valve and custom code, while our methods are now freely-available and segmentation-based. Their analysis created leaflet models, but the valve was primarily modeled as one piece, and did not divide the valves into individual leaflets or assess coaptation. Further comparison of their post-repair CAVC LAVV and our analysis of the native CAVC is discussed in context of anatomy and physiology below, along with other studies.

Papillary Muscle Anatomy—We found that the left sided PM in our pre-repair CAVC cohort had more acute angles in MS relative to the annular plane than normal mitral controls. Notably, Takahashi et al. found that the PM angles relative to the annulus in their post-repair LAVV cohort had a variable relationship to the PM angles in normal controls which appeared dependent on the PM measured(antero-lateral vs. postero-medial), the degree of LAVV regurgitation, and cardiac phase.[23] For the postero-medial PM in MS they found a more acute PM angle in the LAVV groups relative to normal controls. However, for the antero-lateral PM in MS they noted a less acute (greater) PM angle in the LAVV patients with mild regurgitation, compared to those with moderate or greater regurgitation or normal controls. This discrepancy could be due to the differences in cohort (CAVC vs. partial AVC), the repair process, or methodology.

Takahashi et al. did not evaluate the rotational position of the PM. However, in previous work, Chin et al. and Meijboom et al. examined the rotational position of the left atrioventricular valve PM in patients with AVC defects compared to a normal mitral valve using 2D echocardiography with conflicting results.[17, 18] Chin et al. concluded that the antero-lateral PM is shifted posteriorly and inferiorly in the CAVC and the postero-medial PM is in its normal location. In contrast, Mejiboom et al. suggested that the postero-medial PM is displaced away from the septum towards the lateral wall and that the antero-lateral PM is positioned normally. Notably, these groups utilized different methods and reference frames which may have contributed to differences in their findings. In our study, we used 3D adaptations of both of their methods to assure use of the same reference frame for each analysis. Our findings based on 3D analysis suggest that 1) antero-lateral PM is shifted posteriorly and inferiorly (clockwise as viewed from the ventricle) in the CAVC, and 2) the postero-medial PM is shifted superiorly and laterally (counterclockwise as viewed from the ventricle) in CAVC prior to repair compared to normal mitral valves, resulting in a smaller angle between them compared to normal mitral valves. We believe that our 3D analysis avoids many of the pitfalls of 2D analysis, and provides new insights with regard to rotational position of the PM in addition to their angle relative to the annular plane.[23]

Annulus—We have previously reported a comparison of the native CAVC annulus to the normal mitral valve [14]. Our major finding from that study was that the shape of the native, unrepaired CAVC annulus is significantly more planar than the annulus of a normal mitral valve, with an AHWR typical of a dysfunctional mitral valve in the heart.[8] We confirmed those findings in this smaller, but predominantly new cohort. While Takahashi noted differences in regional annular height between normal mitral valves and CAVC LAVV after repair, it is difficult to compare their findings to our analysis directly as we cannot calculate the AHWR from their study.[23] They did not however find a difference in annular

bending angle between repaired LAVV with minimal regurgitation and normal mitral valves in their cohort, which would suggest no difference in annular planarity. However, their cohort had predominantly partial AVC patients, and not exclusively CAVC as in our cohort.

In this study we also found that the total size of the CAVC native annulus is larger than the combined area of the normal mitral and tricuspid valves. This comparison may be confounded by the fact that the ventricular septum occupies part of this area. However, it may represent dilation of atrioventricular valve annular size and ventricular size in response to volume load in the setting of large atrial and ventricular septal defects.

Implications for CAVC Valve Dysfunction

Hemodynamically significant left AVVR after CAVC repair remains a clinical challenge.[1–4] Previous analysis by Takahashi et al. found that significant LAVV regurgitation was associated with leaflet prolapse, larger annular area, and lateral papillary muscle displacement.[23] However, prior to our study there had been only limited 2D and 3D image-based quantitative exploration of associations of native CAVC structure *before* repair to LAVV function after repair. In a 3D study, Bharucha et al. found that more laterally directed PM are associated with post-operative LAVV regurgitation by leveraging multiplane reconstruction and a protractor on the screen.[24] In previous 2D analyses of the CAVC valve prior to repair, Ho et al. found that a smaller angle between the PM (more closely spaced PM) was associated with AVVR, but that a smaller left mural leaflet was not.[12] We could not confirm either of these relationships in our small study.

Our study did identify several new CAVC structural factors of interest with respect to LAVV regurgitation. Lower AHWR of the native CAVC valve in MS prior to repair was associated with moderate or greater left AVVR after repair. This is intriguing as we have previously demonstrated that the median AHWR in CAVC valves is lower than normal mitral valves, and in the range of dysfunctional mitral valves.[14] In this context, we hypothesized that a more planar CAVC annular structure may lead to a more planar shape after repair, which may in turn be relevant to LAVV function after repair of CAVC. [6, 8, 14] However, while Takahashi et al. demonstrated that lower annular height in regions of the annulus after CAVC repair is associated with AVVR, they did not note differences in non-planar angle across regurgitation groups.[23] Their finding is not consistent with association of annular shape to adult and pediatric mitral valve pathology, and it emphasizes the need for larger studies of annular geometry in CAVC using equivalent and open methodology.[8, 15]

Finally, we found that less left-sided AVV coaptation height preoperatively may be associated with LAVV regurgitation post-repair. This is intuitive, as regurgitation is thought to emanate from coaptation defects. However, our sample size is small, and the ability to accurately determine leaflet coaptation height is highly reliant on image quality. Further work will be needed to determine if this is a reliable metric.

Clinical Relevance and Contribution to Future Research

Both our analysis and clinical experience has demonstrated significant heterogeneity in the structure of the atrioventricular valve leaflets in the CAVC population, and association of LAVV structure to function.[23, 24] For example, Colen et al. described a combination of

abnormalities including short chordae and commissural abnormalities in which full closure of the “cleft” between the superior and inferior bridging leaflets can result in LAVV regurgitation.[11] While clinical observations such as these are helpful, generalizing this concept to explore image-derived quantitative phenotypes may be especially powerful in this highly variable population.

Currently the segmentation-based individual leaflet analysis is too slow for routine use. However, emerging techniques including machine learning can rapidly and accurately create models in seconds when provided with sufficient segmented data.[33] Further, techniques such as shape analysis can be used to automatically quantify and compare valve morphologies.[20, 34] The combination of these techniques could allow the rapid characterization of an individual valve within a population, which in turn could inform risk stratification and inform optimal repair strategies.

We have released the tools and CAVC-focused presets used in this analysis open-source within SlicerHeart, an extension for 3D Slicer, which we demonstrate in Videos 1 and 2.[16, 25, 26] We hope that the open-source functionality of our newly released CAVC modeling workflow facilitates application to larger multi-institutional cohorts[27, 28], and in the future catalyzes the creation of physical and computational models to guide CAVC repair.[26, 29–32]

Limitations

Our study is retrospective. While we normalized all metrics to BSA, the patients with CAVC were younger than the patients in the normal mitral group due to the lack of available mitral 3D images in children with echocardiograms demonstrating normal anatomy in the age group undergoing CAVC repair. There is not a clear indication for sedation (to enable optimal 3DE acquisition) in normal children in this age group. However, we have shown that the mitral annular shape (and specifically AHWR) to be highly preserved from neonate to young adult [15], and given the large differences in shape, this age difference is unlikely to influence our conclusions. We examined the annular shape and leaflet metrics at several different points in the cardiac cycle, but not every possible time frame. In future studies, we hope to be able to include all phases of the cardiac cycle leveraging automated methods.[33] We had relatively few patients with significant AVVR, and this clearly limited our power to elucidate more subtle differences across groups. Analysis was done semi-automatically by experienced modelers which requires training, is time-consuming, and contributes to variability. In the future, the development of automated segmentation methods could make this more practical for clinical use.[33, 34] Finally, our study is limited to pre-operative 3D imaging, and post-operative 3DE imaging was unavailable.

CONCLUSIONS

3DE-derived modeling and quantifying the 3D structure of the unrepaired CAVC leaflets, annulus, and PM is feasible using novel software. We demonstrate significant differences in annular, leaflet and PM structure compared to the normal mitral valve. Further research is needed to identify 3D structural associations of valve dysfunction and inform the development of 3D image-based customized repairs in this vulnerable population.

Supplementary Material

Refer to Web version on PubMed Central for supplementary material.

Acknowledgments:

We would like to acknowledge the sonographers at participating institutions for the outstanding images utilized for this research.

Funding:

This work was supported a Pediatric Heart Network Scholars Award (NIH U24 HL135691), NIH 1R01HL153166, NIH NIBIB R01EB021391, Big Hearts to Little Hearts, a CHOP Cardiac Center Innovation Award, The Cora Topolewski Fund at CHOP Pediatric Valve Center, and the CANARIE Research Software foundation.

Abbreviations:

2D	Two-Dimensional
2DE	Two-Dimensional Echocardiography
3D	Three-Dimensional
3DE	Three-dimensional Echocardiography
AHWR	Annular height to valve width ratio
AVC	Atrioventricular canal
AVVR	Atrioventricular Valve Regurgitation
BSA	Body surface area
CAVC	Complete Atrioventricular Canal
CHOP	Children’s Hospital of Philadelphia
DICOM	Digital Imaging in Medicine
Echo	Echocardiography
ED	End-diastole
ES	End-systole
ICC	Intraclass Correlation Coefficient
IRB	Institutional Review Board
LAVV	Left atrioventricular valve
LA	Left anterior CAVC annulus
LP	Left posterior CAVC annulus
MD	Mid-diastole

MS	Mid-systole
PDM	Point Distribution Models
PM	Papillary muscle
SPHARM	Spherical Harmonic

REFERENCES

[1]. Prifti E, Bonacchi M, Baboci A, Giunti G, Krakulli K, Vanini V. Surgical outcome of reoperation due to left atrioventricular valve regurgitation after previous correction of complete atrioventricular septal defect. J Card Surg. 2013;28:756–63. [PubMed: 24224745]

[2]. Stulak JM, Burkhart HM, Dearani JA, Schaff HV, Cetta F, Barnes RD, et al. Reoperations after initial repair of complete atrioventricular septal defect. Ann Thorac Surg. 2009;87:1872–7; discussion 7–8. [PubMed: 19463612]

[3]. Suzuki K, Tatsuno K, Kikuchi T, Mimori S. Predisposing factors of valve regurgitation in complete atrioventricular septal defect. J Am Coll Cardiol. 1998;32:1449–53. [PubMed: 9809961]

[4]. Ten Harkel AD, Cromme-Dijkhuis AH, Heinerman BC, Hop WC, Bogers AJ. Development of left atrioventricular valve regurgitation after correction of atrioventricular septal defect. Ann Thorac Surg. 2005;79:607–12. [PubMed: 15680844]

[5]. Mahmood F, Matyal R. A quantitative approach to the intraoperative echocardiographic assessment of the mitral valve for repair. Anesth Analg. 2015;121:34–58. [PubMed: 26086507]

[6]. Salgo IS, Gorman JH 3rd, Gorman RC, Jackson BM, Bowen FW, Plappert T, et al. Effect of annular shape on leaflet curvature in reducing mitral leaflet stress. Circulation. 2002;106:711–7. [PubMed: 12163432]

[7]. Addetia K, Muraru D, Veronesi F, Jenei C, Cavalli G, Besser SA, et al. 3-Dimensional Echocardiographic Analysis of the Tricuspid Annulus Provides New Insights Into Tricuspid Valve Geometry and Dynamics. JACC Cardiovasc Imaging. 2019;12:401–12. [PubMed: 29153573]

[8]. Lee AP, Hsiung MC, Salgo IS, Fang F, Xie JM, Zhang YC, et al. Quantitative analysis of mitral valve morphology in mitral valve prolapse with real-time 3-dimensional echocardiography: importance of annular saddle shape in the pathogenesis of mitral regurgitation. Circulation. 2013;127:832–41. [PubMed: 23266859]

[9]. Jolley MA, Hammer PE, Ghelani SJ, Adar A, Sleeper LA, Lacro RV, et al. Three-Dimensional Mitral Valve Morphology in Children and Young Adults With Marfan Syndrome. J Am Soc Echocardiogr. 2018;31:1168–77 e1. [PubMed: 30098871]

[10]. Wijdh-den Hamer IJ, Bouma W, Lai EK, Levack MM, Shang EK, Pouch AM, et al. The value of preoperative 3-dimensional over 2-dimensional valve analysis in predicting recurrent ischemic mitral regurgitation after mitral annuloplasty. J Thorac Cardiovasc Surg. 2016;152:847–59. [PubMed: 27530639]

[11]. Colen TM, Khoo NS, Ross DB, Smallhorn JF. Partial zone of apposition closure in atrioventricular septal defect: are papillary muscles the clue. Ann Thorac Surg. 2013;96:637–43. [PubMed: 23702229]

[12]. Ho DY, Katcoff H, Griffis HM, Mercer-Rosa L, Fuller SM, Cohen MS. Left Valvar Morphology Is Associated With Late Regurgitation in Atrioventricular Canal Defect. Ann Thorac Surg. 2020;110:969–78. [PubMed: 32088289]

[13]. Narang H, Rego BV, Khalighi AH, Aly A, Pouch AM, Gorman RC, et al. Pre-surgical Prediction of Ischemic Mitral Regurgitation Recurrence Using In Vivo Mitral Valve Leaflet Strains. Ann Biomed Eng. 2021;49:3711–23. [PubMed: 33837494]

[14]. Nam HH, Dinh PV, Lasso A, Herz C, Huang J, Posada A, et al. Dynamic Annular Modeling of the Unrepaired Complete Atrioventricular Canal Annulus. Ann Thorac Surg. 2022;113:654–62. [PubMed: 33359720]

[15]. Jolley MA, Ghelani SJ, Adar A, Harrild DM. Three-Dimensional Mitral Valve Morphology and Age-Related Trends in Children and Young Adults with Structurally Normal Hearts Using Transthoracic Echocardiography. J Am Soc Echocardiogr. 2017;30:561–71. [PubMed: 28391001]

[16]. Nguyen AV, Lasso A, Nam HH, Faerber J, Aly AH, Pouch AM, et al. Dynamic Three-Dimensional Geometry of the Tricuspid Valve Annulus in Hypoplastic Left Heart Syndrome with a Fontan Circulation. J Am Soc Echocardiogr. 2019;32:655–66 e13. [PubMed: 30826226]

[17]. Chin AJ, Bierman FZ, Sanders SP, Williams RG, Norwood WI, Castaneda AR. Subxyphoid 2-dimensional echocardiographic identification of left ventricular papillary muscle anomalies in complete common atrioventricular canal. Am J Cardiol. 1983;51:1695–9. [PubMed: 6858877]

[18]. Meijboom EJ, Ebels T, Anderson RH, Schasfoort-van Leeuwen MJ, Deanfield JE, Eijgelaar A, et al. Left atrioventricular valve after surgical repair in atrioventricular septal defect with separate valve orifices ("ostium primum atrial septal defect"): an echo-Doppler study. Am J Cardiol. 1986;57:433–6. [PubMed: 3946260]

[19]. Vicory J, Pascal L, Hernandez P, Fishbaugh J, Prieto J, Mostapha M, et al. SlicerSALT: Shape AnaLysis Toolbox. Shape Med Imaging (2018). 2018;11167:65–72. [PubMed: 31032495]

[20]. Vicory J, Herz C, Allemang D, Nam HH, Cianciulli A, Vigil C, et al. Statistical Shape Analysis of the Tricuspid Valve in Hypoplastic Left Heart Syndrome. Cham: Springer International Publishing; 2022. p. 132–40.

[21]. Jolliffe IT, Cadima J. Principal component analysis: a review and recent developments. Philosophical Transactions of the Royal Society A: Mathematical, Physical and Engineering Sciences. 2016;374:20150202.

[22]. Sluysmans T, Colan SD. Theoretical and empirical derivation of cardiovascular allometric relationships in children. J Appl Physiol (1985). 2005;99:445–57. [PubMed: 15557009]

[23]. Takahashi K, Mackie AS, Thompson R, Al-Naami G, Inage A, Rebeyka IM, et al. Quantitative real-time three-dimensional echocardiography provides new insight into the mechanisms of mitral valve regurgitation post-repair of atrioventricular septal defect. J Am Soc Echocardiogr. 2012;25:1231–44. [PubMed: 23022090]

[24]. Bharucha T, Sivaprakasam MC, Haw MP, Anderson RH, Vettukattil JJ. The angle of the components of the common atrioventricular valve predicts the outcome of surgical correction in patients with atrioventricular septal defect and common atrioventricular junction. J Am Soc Echocardiogr. 2008;21:1099–104. [PubMed: 18558474]

[25]. Fedorov A, Beichel R, Kalpathy-Cramer J, Finet J, Fillion-Robin JC, Pujol S, et al. 3D Slicer as an image computing platform for the Quantitative Imaging Network. Magn Reson Imaging. 2012;30:1323–41. [PubMed: 22770690]

[26]. Scanlan AB, Nguyen AV, Ilina A, Lasso A, Cripe L, Jegatheeswaran A, et al. Comparison of 3D Echocardiogram-Derived 3D Printed Valve Models to Molded Models for Simulated Repair of Pediatric Atrioventricular Valves. Pediatr Cardiol. 2018;39:538–47. [PubMed: 29181795]

[27]. Mahony L, Sleeper LA, Anderson PA, Gersony WM, McCrindle BW, Minich LL, et al. The Pediatric Heart Network: a primer for the conduct of multicenter studies in children with congenital and acquired heart disease. Pediatr Cardiol. 2006;27:191–8. [PubMed: 16261271]

[28]. Burns KM, Pemberton VL, Pearson GD. The pediatric heart network: meeting the challenges to multicenter studies in pediatric heart disease. Curr Opin Pediatr. 2015;27:548–54. [PubMed: 26196261]

[29]. Ginty OK, Moore JT, Eskandari M, Carnahan P, Lasso A, Jolley MA, et al. Dynamic, patient-specific mitral valve modelling for planning transcatheter repairs. Int J Comput Assist Radiol Surg. 2019;14:1227–35. [PubMed: 31115756]

[30]. Sacks M, Drach A, Lee CH, Khalighi A, Rego B, Zhang W, et al. On the simulation of mitral valve function in health, disease, and treatment. J Biomech Eng. 2019;141:0708041–07080422.

[31]. Lee CH, Laurence DW, Ross CJ, Kramer KE, Babu AR, Johnson EL, et al. Mechanics of the Tricuspid Valve-From Clinical Diagnosis/Treatment, In-Vivo and In-Vitro Investigations, to Patient-Specific Biomechanical Modeling. Bioengineering (Basel). 2019;6.

[32]. Qin T, Caballero A, Hahn RT, McKay R, Sun W. Computational Analysis of Virtual Echocardiographic Assessment of Functional Mitral Regurgitation for Validation of Proximal

Isovelocity Surface Area Methods. J Am Soc Echocardiogr. 2021;34:1211–23. [PubMed: 34214636]

[33]. Herz C, Pace DF, Nam HH, Lasso A, Dinh P, Flynn M, et al. Segmentation of Tricuspid Valve Leaflets From Transthoracic 3D Echocardiograms of Children With Hypoplastic Left Heart Syndrome Using Deep Learning. Front Cardiovasc Med. 2021;8:735587. [PubMed: 34957233]

[34]. Pouch AM, Aly AH, Lasso A, Nguyen AV, Scanlan AB, McGowan FX, et al. Image Segmentation and Modeling of the Pediatric Tricuspid Valve in Hypoplastic Left Heart Syndrome. Lect Notes Comput Sc. 2017;10263:95–105.

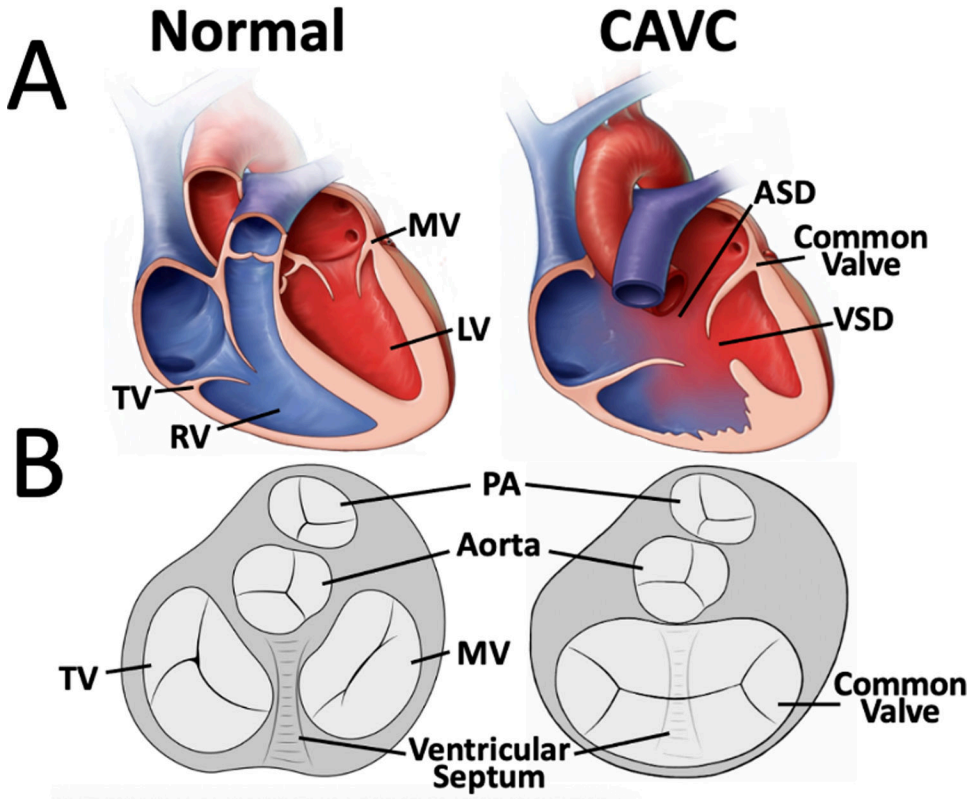

Figure 1. Overview of Normal Anatomy and Complete Atrioventricular Canal Anatomy.

A. Cutaway diagrams of a normal heart and complete atrioventricular canal. B. Schematic diagrams from a ventricular view.

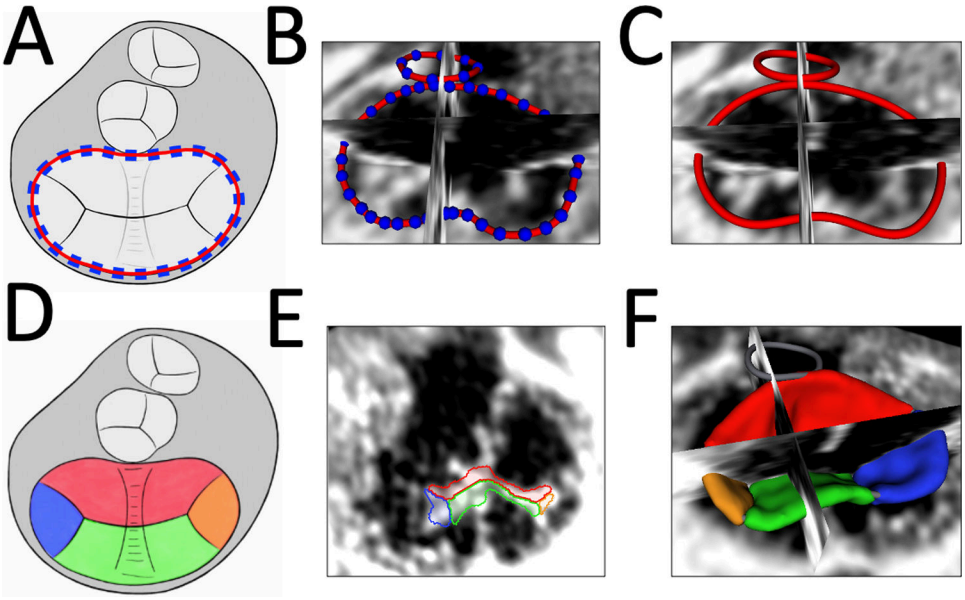

Figure 2. Visualization and Modeling of CAVC Annuli and Leaflets in Mid-Systole.

A. Schematic of CAVC annular modeling; **B**. Creation of CAVC Annular Curve; **C**. Smoothed CAVC annulus curve visualized in SlicerHeart; **D**. Schematic of CAVC leaflet modeling from ventricular view; **E**. 2D ventricular view of CAVC valve segmentation in SlicerHeart from ventricular view; **F**. CAVC leaflet model visualized from atrial view in with 2D slice intersections in SlicerHeart. (Red = superior bridging leaflet, Blue = right mural leaflet, Green = inferior bridging leaflet, Orange = left mural leaflet).

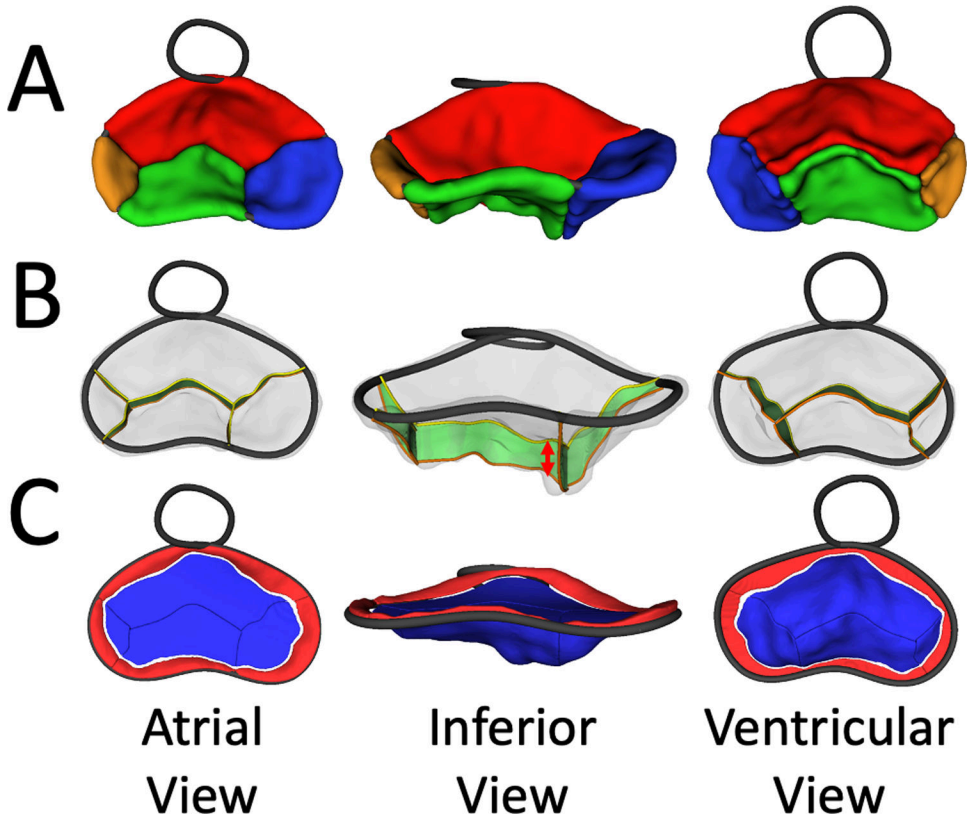

Figure 3. CAVC Leaflet Quantification.

A. Visualization of Segmented CAVC valve from atrial (left), inferior (middle) and ventricular view (right) in SlicerHeart; **B**. Visualization of CAVC coaptation surface areas from atrial (left), inferior (middle) and ventricular view (right) in SlicerHeart; **C**. Visualization of leaflet billow (red) and tenting (blue) from atrial (left), inferior (middle) and ventricular view (right) in SlicerHeart.

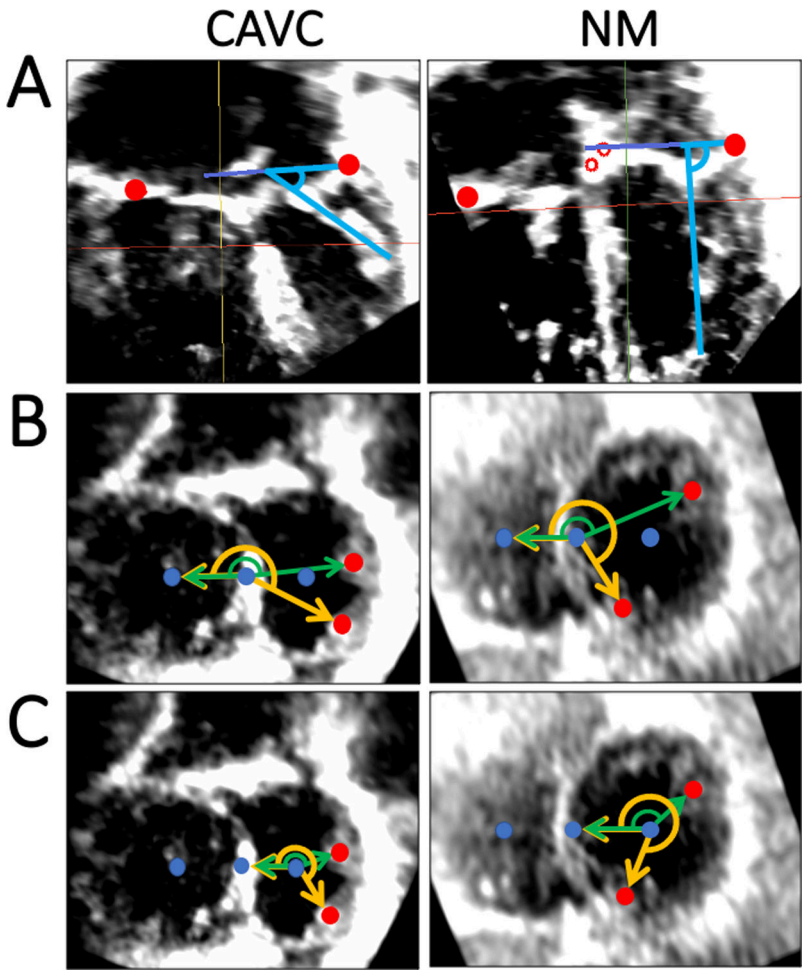

Figure 4. Papillary Muscle Angle Quantification in CAVC and Normal Mitral Valves.

A. Papillary muscle angle relative to annulus plane in CAVC and normal mitral; **B**. "Septal Point" based rotation angle measurement in CAVC and normal mitral valves. Reference vector is perpendicular to the septal plane, and papillary muscle base points are projected to the common CAVC and common normal mitral/tricuspid valve plane; **C**. "Center point" based rotation angle measurement in CAVC and normal mitral valves. Reference vector is perpendicular to the center plane, and papillary muscle base points are projected to the left CAVC and mitral valve plane. CAVC = Complete atrioventricular canal, NM = Normal Mitral.

Video 1:
Overview of CAVC Annular Modeling and Segmentation in SlicerHeart

Video 2:
Overview of Leaflet, Annular, and Papillary Muscle Quantification in SlicerHeart

Video 3:

Demonstration of Mean CAVC Shape and Morphologic Variation using Principal Component Analysis

Table 1.

Demographics

Variable	Normal Mitral n=18	CAVC n=35
Age (years)	3.0 [0.0–4.4]	0.3 [0.2–0.3]
Female gender (n, %)	9 (50%)	20 (57%)
Height (cm)	95.0 [51.8–109.1]	58 [50.9–60.8]
Weight (kg)	14.5 [3.6–18.5]	4.4 [3.4–5.1]
BSA (m^2)	0.62 [0.23–0.75]	0.27 [0.23–0.29]
Heart Rate (bpm)	99 [83–116]	136 [126–143]
Rastelli Type		
A (n, %)		20 (57%)
C (n, %)		15 (43%)
Trisomy 21 (n, %)		29 (83%)
Pre-repair Qualitative Ventricular Function of Native CAVC		
Normal (n, %)	100%	32 (91%)
Mildly diminished (n, %)		2 (6%)
Moderately diminished (n, %)		1 (3%)
Pre-Repair AVV Regurgitation		
Mild or less (n, %)		25 (71%)
Moderate or greater (n, %)		10 (29%)
Post-Repair Right AVV Regurgitation		
Mild or less (n, %)		28 (80%)
Moderate or greater (n, %)		6 (17%)
Post-Repair Left AVV Regurgitation*		
Mild or less (n, %)		21 (60%)
Moderate or greater (n, %)		13 (37%)
Frame rate (Hz)	31 [25–37]	34 [33–43]

BSA = body surface area; AVV = atrioventricular valve.

Data are expressed as median [interquartile range] or as a number (percentage).

*only 34 patients underwent CAVC repair

Table 2.

CAVC Leaflet Changes Throughout the Cardiac Cycle n=35

Variable	----------SYSTOLE---------- End-Diastole	Mid-Systole	End-Systole	Max Change (%)	*p* Value
Total Leaflet Area (cm ^{2} /m ^{2})					
Total	45.20 [40.87, 51.33]	38.90 [34.91, 46.37]	39.20 [34.22, 46.75]	21.4 [13.0, 27.9]	<0.001 *
Inferior Bridging Leaflet	13.64 [10.72, 14.97]	11.38 [8.48, 13.21]	10.84 [8.96, 13.21]	26.5 [15.9, 39.4]	<0.001 *
Left Mural Leaflet	6.61 [5.43, 7.61]	5.34 [4.25, 6.67]	5.52 [4.24, 6.38]	34.4 [23.6, 47.3]	0.004 *
Right Mural Leaflet	7.71 [6.12, 8.73]	6.73 [5.59, 8.25]	6.96 [5.08, 8.06]	32.9 [21.3, 51.9]	0.002 *
Superior Bridging Leaflet	19.34 [16.07, 22.64]	16.04 [14.08, 18.67]	16.03 [13.69, 18.41]	26.6 [14.8, 38.2]	<0.001 *
Atrial Leaflet Area (cm ^{2} /m ^{2})					
Total	30.92 [28.46, 35.62]	26.00 [23.90, 32.25]	26.22 [23.10, 31.90]	21.0 [14.9, 27.9]	<0.001 *
Inferior Bridging Leaflet	8.62 [6.57, 9.85]	7.68 [5.72, 8.36]	7.15 [5.79, 8.62]	23.3 [15.3, 46.8]	<0.001 *
Left Mural Leaflet	4.33 [3.52, 5.66]	3.42 [3.00, 4.31]	3.44 [2.71, 4.66]	33.1 [22.5, 46.7]	<0.001 *
Right Mural Leaflet	5.36 [4.38, 6.20]	4.65 [3.64, 5.28]	4.52 [3.71, 5.73]	37.4 [22.3, 49.7]	<0.001 *
Superior Bridging Leaflet	13.94 [11.37, 16.04]	11.34 [9.75, 13.95]	10.96 [9.83, 12.98]	21.9 [12.2, 39.6]	<0.001 *
Relative Leaflet Area (%)					
Inferior Bridging Leaflet	30 [26, 31]	28 [25, 30]	28 [25, 29]	17.5 [11.2, 34.0]	0.918
Left Mural Leaflet	15 [12, 16]	14 [12, 17]	15 [12, 16]	29.5 [15.8, 40.5]	0.690
Right Mural Leaflet	17 [14, 19]	17 [15, 20]	17 [15, 20]	22.2 [11.1, 47.1]	0.147
Superior Bridging Leaflet	41 [37, 45]	41 [38, 43]	40 [36, 45]	13.5 [7.5, 18.5]	0.196
Billow Volume (cm ^{3} /m ^{2})					
Total	0.55 [0.42, 0.69]	0.63 [0.50, 0.96]	0.85 [0.58, 1.27]	70.5 [33.9, 133.6]	<0.001 *
Inferior Bridging Leaflet	0.06 [0.04, 0.08]	0.09 [0.06, 0.15]	0.09 [0.06, 0.15]	111.1 [63.7, 203.1]	<0.001 *
Left Mural Leaflet	0.05 [0.03, 0.07]	0.07 [0.04, 0.10]	0.09 [0.06, 0.11]	119.0 [69.6, 175.3]	<0.001 *
Right Mural Leaflet	0.08 [0.05, 0.11]	0.09 [0.06, 0.18]	0.11 [0.06, 0.18]	108.1 [31.6, 219.9]	0.030 *
Superior Bridging Leaflet	0.14 [0.11, 0.21]	0.19 [0.14, 0.30]	0.29 [0.14, 0.44]	87.7 [46.6, 227.1]	<0.001 *
Billow Height (cm/m)	0.26 [0.22, 0.32]	0.28 [0.23, 0.32]	0.31 [0.27, 0.37]	40.0 [20.0, 61.0]	0.030 *

Variable	SYSTOLE				
	End-Diastole	Mid-Systole	End-Systole	Max Change (%)	*p* Value
Tenting Volume (cm^3/m^2)					
Total	3.52 [2.36, 5.94]	1.82 [0.61, 3.15]	1.29 [0.42, 2.44]	196.5 [128.4, 538.9]	<0.001*
Inferior Bridging Leaflet	1.36 [0.79, 2.29]	0.56 [0.21, 1.15]	0.44 [0.12, 0.99]	228.9 [150.2, 471.8]	<0.001*
Left Mural Leaflet	0.19 [0.12, 0.35]	0.07 [0.05, 0.14]	0.06 [0.01, 0.11]	284.9 [168.8,1428.3]	<0.001*
Right Mural Leaflet	0.34 [0.20, 0.46]	0.11 [0.03, 0.26]	0.11 [0.02, 0.24]	383.3 [158.0,3073.5]	<0.001*
Superior Bridging Leaflet	1.60 [1.08, 2.76]	0.86 [0.23, 1.65]	0.52 [0.14, 1.20]	218.9 [115.5, 682.5]	<0.001*
Tenting Height (cm/m)	1.20 [0.76, 1.52]	0.73 [0.39, 0.94]	0.73 [0.45, 0.87]	88.6 [65.3, 125.4]	<0.001*

Values listed are Median [IQR]

* $p<0.05$

Table 3.

Papillary Muscle Analysis

Papillary Muscle Analysis in Mid-Systole	Normal Mitral n=18	Left Side CAVC n=34	p Value
PM Base to Annulus Plane Angle (degrees)			
Antero-lateral	79 [76–82]	55 [44–64]	<0.001 *
Postero-medial	77 [75–80]	57 [50–63]	<0.001 *
Septal Point Based PM Rotation Angle (degrees)			
Antero-lateral	176 [167–184]	192 [184–196]	0.001 *
Postero-medial	240 [233–249]	220 [213–233]	<0.001 *
Center Point Based PM Rotation Angle (degrees)			
Antero-lateral	153 [135–168]	201 [188–213]	<0.001 *
Postero-medial	276 [259–285]	247 [233–258]	<0.001 *
Septal Point Based PM Rotation Angle Difference (degrees)	67 [58–79]	32 [28–37]	<0.001 *
Center Point Based PM Rotation Angle Difference (degrees)	122 [103–133]	49 [35–56]	<0.001 *
Normalized Papillary Muscle Base Point Distance (cm/m)	1.9 [1.7–2.2]	1.9 [1.5–2.2]	0.92
Total Annular Area (cm^2/m^2)	11.9 [10.8–13.4] *(TV +NM)	19.6 [18.0–23.7] *whole CAVC	<0.001 *

Septal Point Based PM Rotation Angle Difference = Postero-medial septal point based PM rotation angle – antero-lateral septal point based PM rotation angle

CenterPoint Based PM Rotation Angle Difference = Postero-medial center point based PM rotation angle – antero-lateral center point based PM rotation angle

Values listed are Median [IQR]

*p<0.05

Table 4.

Comparison of CAVC Trivial/Mild AVVR vs. Moderate/Severe AVVR;

	Pre-Repair AVVR			Post-Repair Left AVVR		
Variable	**Trivial/Mild (n=25)**	**Moderate/Severe (n=10)**	***p* Value**	**Trivial/Mild (n=21)**	**Moderate/Severe (n=13)**	***p* Value**
PM Base to Annulus Plane Angle in MS (degrees)						
Antero-lateral	54 [43–64]	60 [51–63]	0.780	55 [42–61]	54 [44–63]	0.650
Postero-medial	57 [49–63]	57 [55–62]	0.955	58 [52–63]	57 [50–63]	0.897
Septal Point Based PM Rotation Angle in MS (degrees)						
Antero-lateral	191 [184–195]	195 [186–196]	0.533	189 [184–195]	196 [190–199]	0.161
Postero-medial	220 [210–232]	222 [215–237]	0.299	215 [212–228]	227 [220–235]	0.136
Center Point Based PM Rotation Angle in MS (degrees)						
Antero-lateral	199 [188–210]	204 [194–216]	0.564	196 [187–207]	207 [199–215]	0.281
Postero-medial	245 [231–256]	254 [240–261]	0.162	244 [232–257]	254 [243–260]	0.191
Septal Point Based PM Rotation Angle Difference in MS (degrees)	32 [29–36]	31 [27–44]	0.850	30 [24–35]	33 [31–39]	0.161
Center Point Based PM Rotation Angle Difference in MS (degrees)	49 [35–55]	48 [40–63]	0.496	43 [35–56]	52 [40–60]	0.439

Septal Point Based PM Rotation Angle Difference = Postero-medial septal point based PM rotation angle – antero-lateral septal point based PM rotation angle

CenterPoint Based PM Rotation Angle Difference = Postero-medial center point based PM rotation angle – antero-lateral center point based PM rotation angle

Values listed are Median [IQR]

* $p<0.05$

Table 5.

Comparison of CAVC Trivial/Mild AVVR vs. Moderate/Severe AVVR;

	Pre-Repair AVVR			Post-Repair Left AVVR		
Variable	**Trivial/Mild (n=25)**	**Moderate/Severe (n=10)**	***p* Value**	**Trivial/Mild (n=21)**	**Moderate/Severe (n=13)**	***p* Value**
Total Annulus Area (cm^2/m^2)						
Mid-systole	19.79 [18.11–21.80]	17.80 [16.93–21.91]	0.141	19.79 [16.75–23.95]	18.76 [18.07–21.26]	0.753
End-systole	19.50 [17.59–21.70]	18.07 [16.44–21.29]	0.339	19.50 [17.02–22.86]	18.39 [17.32–19.52]	0.600
Total Annulus Circumference (cm/m)						
Mid-systole	16.49 [16.16–18.16]	15.39 [15.30–17.49]	0.113	16.47 [15.36–18.16]	16.42 [16.13–17.71]	1
End-systole	16.87 [15.93–17.71]	15.78 [15.10–17.19]	0.174	16.87 [14.94–18.16]	16.03 [15.93–17.30]	0.917
Total Annulus Height (cm/m)						
Mid-systole	0.69 [0.56–0.81]	0.59 [0.39–0.66]	0.028*	0.70 [0.60–0.81]	0.60 [0.48–0.67]	0.012*
End-systole	0.65 [0.59–0.95]	0.52 [0.50–0.59]	0.005*	0.64 [0.59–0.96]	0.58 [0.50–0.71]	0.082
Total AHWR						
Mid-systole	0.19 [0.15–0.23]	0.17 [0.12–0.19]	0.240	0.20 [0.17–0.23]	0.16 [0.12–0.18]	0.013*
End-systole	0.20 [0.18–0.24]	0.14 [0.14–0.17]	0.011*	0.20 [0.18–0.24]	0.16 [0.14–0.18]	0.065
Billow Volume (cm^3/m^2)						
Mid-systole	0.64 [0.58–1.08]	0.49 [0.38–0.64]	0.018*	0.71 [0.51–1.08]	0.61 [0.41–0.64]	0.205
End-systole	0.90 [0.64–1.35]	0.58 [0.37–0.80]	0.022*	1.01 [0.58–1.39]	0.78 [0.58–0.86]	0.326
Tenting Volume (cm^3/m^2)						
Mid-systole	1.05 [0.56–2.69]	2.41 [0.91–4.37]	0.255	1.38 [0.54–2.98]	2.48 [0.65–3.31]	0.727
End-systole	0.95 [0.40–2.03]	2.22 [0.91–4.20]	0.122	1.28 [0.44–2.30]	1.30 [0.40–3.59]	0.753
Minimum Left Side Coaptation Height (cm/m)						
Mid-systole	0.19 [0.17–0.22]	0.17 [0.13–0.26]	0.547	0.20 [0.18–0.22]	0.15 [0.14–0.18]	0.040*
End-systole	0.19 [0.17–0.21]	0.20 [0.17–0.23]	0.913	0.20 [0.17–0.24]	0.18 [0.17–0.19]	0.103
Mean Left Side Coaptation Height (cm/m)						
Mid-systole	0.47 [0.40–0.52]	0.50 [0.44–0.54]	0.321	0.49 [0.43–0.53]	0.43 [0.38–0.48]	0.120
End-systole	0.47 [0.39–0.53]	0.45 [0.41–0.49]	0.756	0.49 [0.39–0.54]	0.44 [0.39–0.47]	0.082
Left Side Coaptation Area (cm^2/m^2)						
Mid-systole	2.48 [2.17–2.80]	2.51 [2.34–3.08]	0.397	2.52 [2.20–2.80]	2.45 [2.17–2.95]	0.625

Variable	Pre-Repair AVVR: Trivial/Mild (n=25)	Pre-Repair AVVR: Moderate/Severe (n=10)	*p* Value	Post-Repair Left AVVR: Trivial/Mild (n=21)	Post-Repair Left AVVR: Moderate/Severe (n=13)	*p* Value
End-systole	2.33 [1.89–2.81]	2.47 [2.01–2.82]	0.957	2.46 [1.85–2.91]	2.11 [1.98–2.60]	0.462

AHWR = annular height to width ratio; PM = papillary muscle; MS = mid-systole

Annulus Width: For CAVC = LA-LP Distance; For Normal Mitral = AL-PM distance;

Left AHWR = For CAVC = Left annulus height / LA-LP Distance; For Normal Mitral = Total annulus height / AL-PM distance

Total AHWR = Total annulus height / LA-LP Distance; For Normal Mitral = Total annulus height / AL-PM distance

Values listed are Median [IQR]

* $p<0.05$